Effect of spacer configuration on the characteristics of FO membranes: Alteration of permeation characteristics by membrane deformation and concentration polarization

Chulmin Lee[a], Jaewon Jang[a], Nguyen Thanh Tin[a], Suhun Kim[a],Chuyang Y. Tang[b,c,d], In S Kim[a.*]

[a] School of Earth Sciences and Environmental Engineering, Gwangju Institute of Science and Technology (GIST), 123 Cheomdangwagi-ro, Buk-gu, Gwangju 61005, South Korea

[b] Department of Civil Engineering, the University of Hong Kong, Pokfulam, Hong Kong

[c] UNESCO Centre for Membrane Science and Technology, School of Chemical 9 Engineering, University of New South Wales, Sydney, New South Wales 2052, 10 Australia 11

[d] UNSW Water Research Centre, School of Civil and Environmental Engineering, 12 University of New South Wales, Sydney, New South Wales 2052, Australia

*Corresponding author: School of Earth Sciences and Environmental Engineering, Gwangju Institute of Science and Technology (GIST), 123 Cheomdangwagi-ro, Buk-gu, Gwangju 61005, South Korea

+82-62-715-2436, iskim@gist.ac.kr

TOC

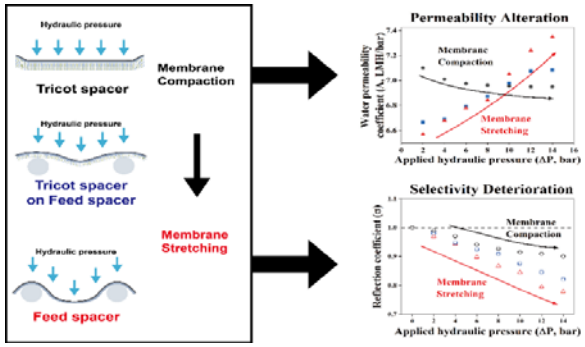
Hydraulic pressure
Tricot spacer
Membrane Compaction
Hydraulic pressure
Tricot spacer on Feed spacer
Membrane Stretching
Hydraulic pressure
Feed spacer
Permeability Alteration
Membrane Compaction
Membrane Stretching
Water permeability coefficient (A, LMH/bar)
Applied hydraulic pressure (ΔP, bar)
Selectivity Deterioration
Membrane Compaction
Membrane Stretching
Reflection coefficient (σ)
Applied hydraulic pressure (ΔP, bar)

Abstract

Membrane deformation is a significant problem in osmotically driven membrane processes, as it restricts practical operating conditions and reduces overall process performance due to unfavorable alteration of membrane permeation characteristics. In this respect, a spacer plays a crucial role, as it dictates the form and extent of membrane deformation in association with concentration polarization (CP), which is also influenced by spacer-induced hydrodynamic behavior near the membrane surface. These two roles of spacers on membrane permeation characteristics are inherently inseparable with the coexistence of hydraulic and osmotic pressures. Here, we suggest a novel analytical method to differentially quantify the proportions of effective osmotic pressure drop caused by membrane deformation and CP. Furthermore, we tested two different FO membranes with three different spacer configurations to define and discuss different forms of membrane deformation and their effects on membrane permeation characteristics. The differential analysis revealed the effect of spacer configuration on effective osmotic pressure drop in membrane deformation (up to ~ 201% of variation) is much greater than that in CP (up to ~20.1% of variation). In addition, a combined configuration of a feed spacer and tricot spacer demonstrated its ability of mitigating membrane deformation with lower selectivity loss and channel pressure drop under pressurization.

Introduction

Osmotically driven membrane processes (ODMPs), such as forward osmosis (FO), pressure-assisted forward osmosis (PAFO) and pressure-retarded osmosis (PRO), have been studied extensively in recent years for water and energy-associated applications[1,2]. The low-pressure nature of FO and PAFO offers potential energy savings in niche applications where draw solution regeneration is not required (or can be achieved using alternative energy sources with low cost)[1,3,4]. FO and PAFO also show more stable flux behavior than pressure-driven membrane processes, as demonstrated by numerous bench-scale tests[5-7]. In parallel, bench-scale PRO experiments often show highly attractive power densities for harvesting salinity gradient power[2]. Nevertheless, recent pilot tests[8-12] using commercial spiral wound modules showed much poorer performance than expected due to deformation of the membranes and spacer-filled channels inside the modules.

Detailed analysis revealed membrane deformation as one of the major critical limiting factors during ODMP operation[13,14]. In PRO, the pressure in the draw solution is often greater than 10 bar[11,15]. Similarly, a maximum applied pressure of 6 bar has been reported for PAFO[16]. Even in FO, where the applied pressure is theoretically zero, a pilot study reported a hydraulic pressure of > 2 bar at the inlet to the draw channel for membrane elements arranged in series[17] due to the hydraulic resistance of the flow channel. Unbalanced pressure across the membrane can cause severe membrane deformation and blockage of flow channels (Figure 1a), which in turn lead to greater pressure drop in the flow channels. This pilot study further demonstrated that the maximum operable number of serially connected elements in FO operation is limited by this draw channel pressure drop[17]. Furthermore, membrane deformation may also result in severe deterioration of the separation properties as well as unfavorable mass transfer

conditions[13,15,18].

Concentration polarization (CP) is another inevitable phenomenon that significantly reduces process performance in ODMPs by decreasing the effective osmotic pressure[19]. Membrane deformation and CP are similar in that both are dictated by spacer geometry[20]; however, they are inherently dependent on each other and inseparable because hydraulic and osmotic pressures always coexist regardless of process type in actual module-scale operation. To critically understand the complex mechanisms of membrane deformation and CP, it is necessary to quantitatively and differentially analyze effective osmotic pressure loss by these two different causes because the extent, applied direction and ratio of osmotic and hydraulic pressures are different for different operating conditions and processes.

In the current study, alteration of membrane separation properties and transport mechanisms is investigated in association with differentiating membrane deformation and CP under different spacer configurations. A conventional solution-diffusion (S-D) model-based characterization method and thermodynamics-based novel characterization method are comparably analyzed to reveal complex mechanisms of water and solute transport with regard to membrane deformation and CP.

Materials and Methods

Membranes

Two commercial osmotic membranes were used in the current study. Thin-film composite polyamide membrane PA-TFC (Toray Chemical Korea Inc., South Korea) consists of a polyamide active layer, a polysulfone support layer, and a polyester support mesh embedded in the polysulfone layer. Cellulose triacetate membrane CTA-ES2 was purchased from Hydration Technology Innovations Inc. (US). This membrane also has an embedded polyester support mesh, and one side of the membrane is thermally treated to form an active layer during the fabrication process. Compared to PA-TFC, which has a relatively flat membrane surface with a constant thickness of ~1.2 mm, CTA-ES2 has varying thickness in the range of 0.63~0.93 mm due to the embedded PET mesh (Figure S1).

Spacer types and configurations

A diamond-shaped feed spacer (thickness of ~ 1.2 mm) and tricot fabric spacer (thickness of ~ 0.2 mm) were both extracted from a spiral wound FO element (CSM FO-8040, Toray Chemical Korea Inc., South Korea). The thickness of the feed spacer and tricot fabric spacer were measured by using a digital caliper with a precision of 0.01 mm. The detailed dimensions and images of these spacers are shown in Figures S1 and S3. Three spacer configurations were used (Figure 1a): (i) tricot spacer only (TS), (ii) feed spacer only (FS), and (iii) both tricot spacer and feed spacer (TS+FS). For a fair comparison, the total height of each spacer configuration was kept constant as 1.4 mm for (FS: 1 feed spacer on top and 1 tricot spacer on the bottom,

TS+FS: 1 tricot spacer on top and 1 feed spacer on the bottom, TS: 7 sheets of tricot spacers). The gap between spacer and channel height was filled by padding several plastic plates at the bottom of the channel. These configurations lead to different spacer-induced membrane deformations under pressurized conditions. Specifically, the membrane is more evenly compressed onto the tricot spacer due to its flat geometry and smaller opening size (which reduces the unsupported span of the membrane). In contrast, the membrane is stretched into the relatively wide openings of the feed spacer. An intermediate deformation condition is created by the combined use of the tricot spacer and feed spacer. According to previous papers[44,45], this combined configuration was employed in a commercial 8 inch FO spiral-wound element (Toray, CSM FO-8040). Throughout all the experiments a feed spacer was constantly used to resolve the effect of spacer-induced axial channel pressure drop and CP in the feed channel. The channel Reynolds number (Re_{ch})[46] computed based on feed spacer geometry in this study was 33.42 (diameter of feed spacer filament is ~0.5 mm), which assures the flow regime in this study falls into the laminar flow. Tricot spacer only configuration (TS) and combined spacer configuration (TS+FS) are most likely to yield lower Re_{ch} due to its high channel porosity.

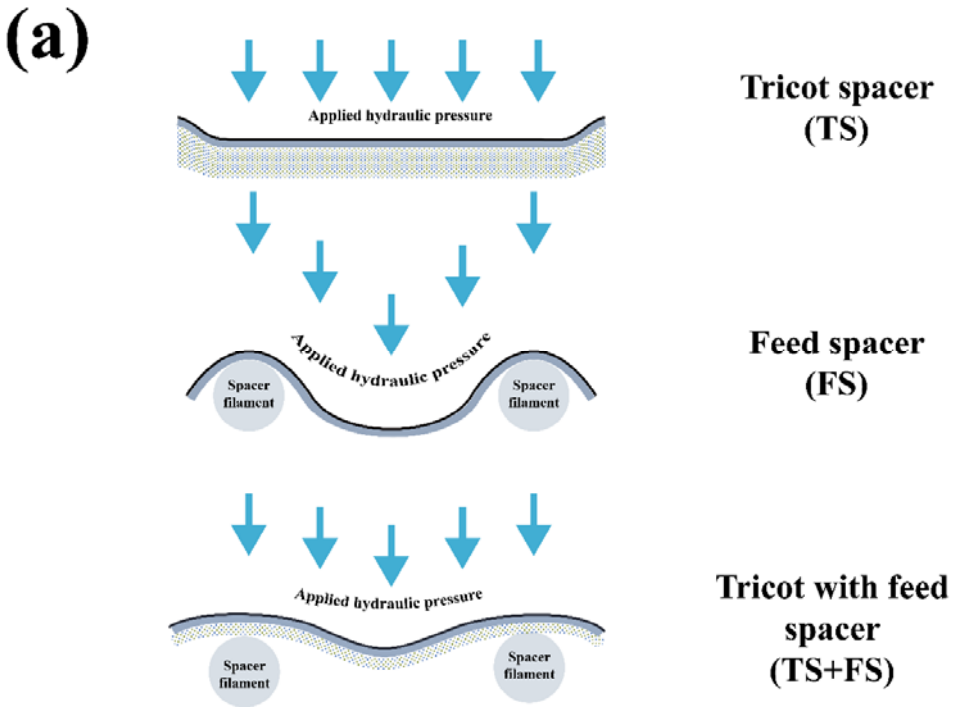

120

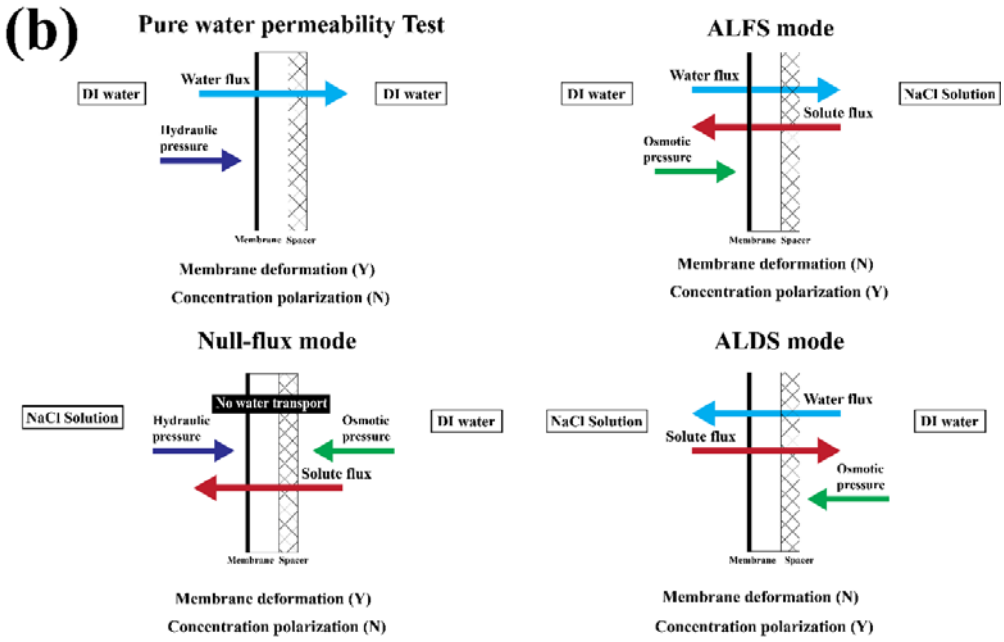

121

122 **Figure 1.** (a) Illustrations of spacer configurations used in this study and their associated
123 membrane deformation; (b) schematic diagrams of the four operation modes and the presence
124 of membrane deformation and CP in each mode.

Membrane performance tests

Figure 1(b) illustrates the four different operation modes used in this study (also see Supporting Information S4 for a detailed schematic diagram of the laboratory-scale experimental setup):

- Pure water permeability test. In this test, deionized (DI) water was used in both feed and draw solution channels to strictly eliminate the presence of osmotic pressure. To take into account precompaction or prestretching of the membrane, each membrane was pressurized under different spacer configurations for 2 h at each designated pressure point. Then, the membrane flux was tested at 100%, 75%, 50% and 25% of the designated pressure with a filtration duration of 5 min at each pressure step. For example, when 2 bar was the designated pressure point, the membrane was first pressurized under 2 bar for 2 h, and the water flux was measured immediately at 2.0, 1.5, 1.0 and 0.5 bar for 5 min, respectively. The water permeability was calculated as the slope of these 4 points.

- FO tests in the active layer facing feed solution orientation (ALFS) and the active layer facing draw solution orientation (ALDS). Both tests were performed under nonpressurized conditions (less than 0.005 bar of channel pressure drop for both feed and draw solution channels). NaCl solution and DI water were used as the draw solution and feed solution, respectively. The water flux was driven by the osmotic pressure difference across the membrane. In the ALFS, the draw solution is placed on the porous substrate side such that a dilutive internal concentration polarization (ICP) occurs. In contrast, the placement of the draw solution on the active layer side in the ALDS results in a concentrative ICP that induces the reverse diffusion of the draw solutes into the

substrate. According to the literature, the ICP is more severe in the ALFS than the ALDS. In the current study, water and solute fluxes were calculated from mass and conductivity changes in the feed solution.

- Null-flux modes. In these modes, the membrane was characterized using null-flux mode, where hydraulic pressure and osmotic pressure act in opposite directions to generate zero water flux (i.e., zero change in water mass). For example, if 2 bar was the designated pressure point, the equivalent draw solution concentration (0.0476 M) was used to generate 2 bar of osmotic pressure. Then, to create zero water permeation, hydraulic pressure was applied in the opposite direction of osmotically driven water permeation. Since the water flux was zero, only the solute flux was measured in this test mode. The Staverman reflection coefficient[21] was derived using Equation S11 to evaluate osmotic pressure loss solely by membrane deformation (no water transport arguably induces negligible occurrence of CP). Before each test under null-flux mode, 2 h of membrane pressurization was conducted in designated pressure conditions to consider the predeformation of the membrane.

Uniaxial tensile test for mechanical strength of membrane

To investigate the correlation between mechanical strength and spacer-induced membrane deformation, a uniaxial tensile test was conducted using a universal testing machine (TEST ONE, Product: TO-100-IC). Specimens of PA-TFC and CTA-ES2 membranes in dried and wet states were prepared according to standard method[33] (ASTM D638: Standard Test Method for Tensile Properties of Plastics) and tested at a displacement speed of 10 mm/min. Ultimate

169 tensile strength (UTS, MPa), elastic modulus (MPa) and elongation at break (%) were
170 computed based on the stress-strain curve of each specimen (Table S1).

171

172

Results and Discussion

Alteration of permeation mechanism due to membrane deformation and concentration polarization

Pure water permeability is normally determined as the slope composed of multiple water flux points measured at different hydraulic pressures using DI water. However, water permeability can vary depending on the spacer and the extent of hydraulic pressure due to structural deformation of the membrane and the resultant permeation mechanism. To examine permeability variation depending on the hydraulic pressure and spacer configuration, a pure water permeability test was conducted for the aforementioned three spacer configurations in the given range of hydraulic pressure. Figure 2 illustrates an example of alteration of water permeability (i.e., change in slope) under 2 hours of membrane compaction with hydraulic pressures of 2 and 12 bar for PA-TFC and CTA-ES2 membranes. The TS configuration shows a slight decline in the slope, while the slopes increase for the TS+FS and FS configurations.

For clear illustration, these water permeability changes are plotted in Figure 3(a) and 3(b). Compared to the TS configuration, the TS+FS and FS configurations resulted in lower initial permeability, which can be explained by the greater shadow effect (i.e., reduction in effective membrane area) in the presence of spacers[29]. For both PA-TFC and CTA-ES2 membranes, the TS configuration shows a modest decreasing trend of water permeability. In contrast, the TS+FS and FS configurations show a steep increasing trend. This disparity in performance indicates that the TS and other two configurations have different forms of membrane deformation. In the TS configuration, the membrane is evenly compacted onto the relatively

flat and rigid tricot spacer, leading to a densified membrane structure and thus increasing membrane resistivity to water permeation. In the TS+FS and FS configurations, the membrane elongates due to the open structure of the feed spacer. As a result of this tensile stretching, the membrane becomes more permeable to water.

Although the two membranes show similar overall trends, their extents of variation were noticeably different, particularly when the membranes were stretched. For example, the water permeability of PA-TFC increased up to 12.9% in the FS configuration, which was much lower than the corresponding change for CTA-ES2 (an increase of 55.5%) under identical testing conditions. The better tolerance of PA-TFC to tensile stretching can be explained by the flexibility of the polyamide active layer for tensile stretching[30].

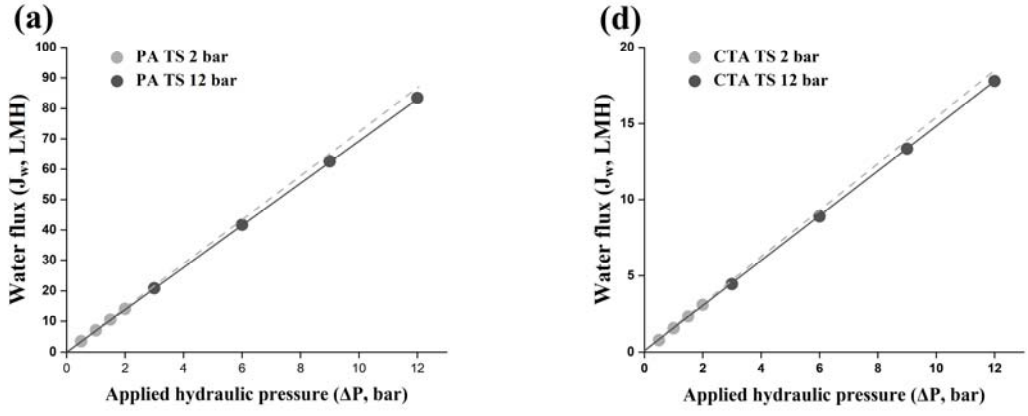

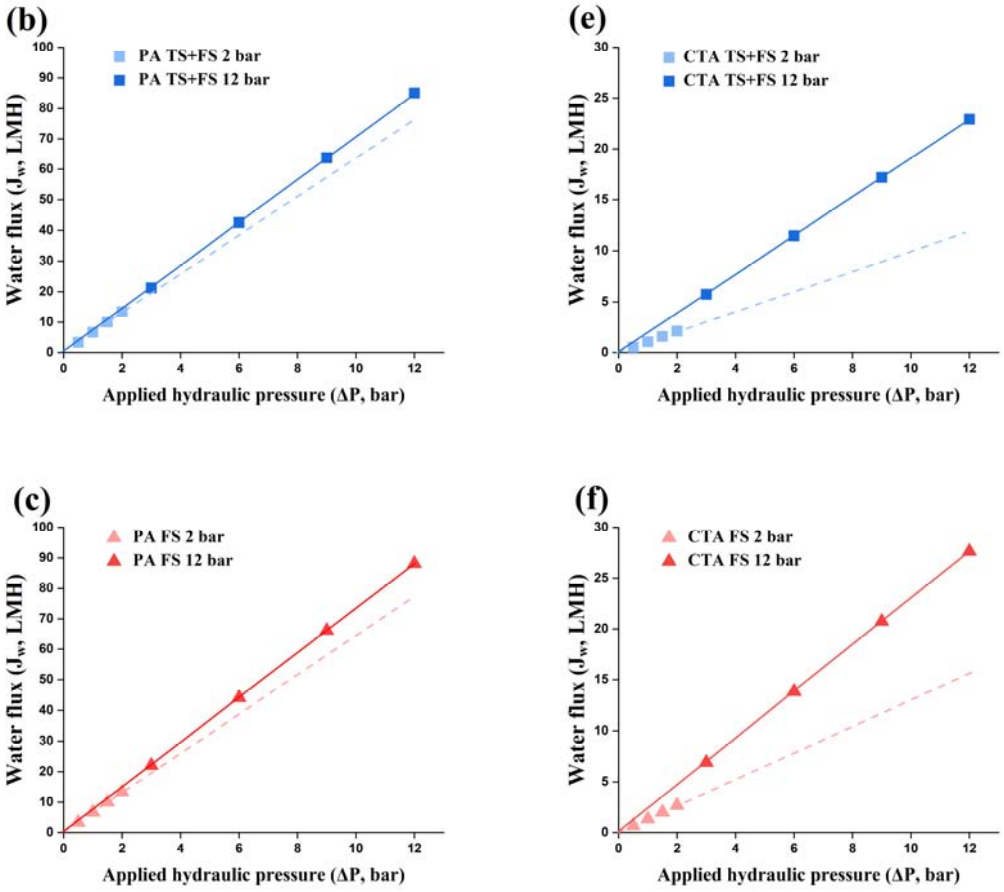

Figure 2. Alteration of pure water permeability under effect of membrane compaction or stretching depending on spacer configuration for PA-TFC membrane (a, b and c) and CTA-ES2 membrane (d, e and f). Pressure specified in legeneds represent hydraulic pressure employed for 2 hours of compaction/stretching depending on spacer configuration.

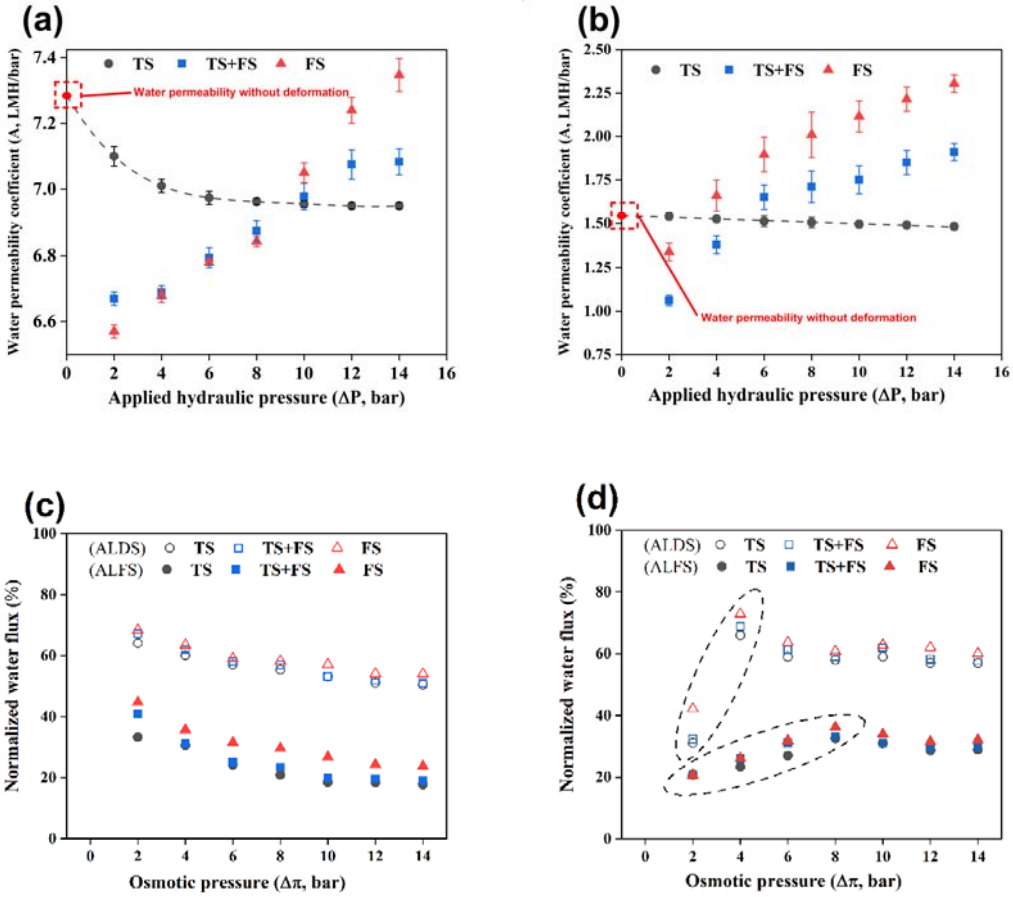

Figure 3. Alteration of water permeability coefficient (A) under pressurized conditions for three spacer configurations, TS, TS+FS, and FS, for (a) PA-TFC and (b) CTA-ES2. Normalized water flux determined by pure water permeability in nondeformed conditions with different spacer configurations for (c) PA-TFC membrane and (d) CTA-ES2 membrane.

With current measurement technology, it is not viable to quantify the proportion of how much water flux declines due to CP solely by experimental methods. However, using an empirical relation between hydraulic pressure and water permeability, as shown in Figure 3(a), the water permeability under nondeformed conditions can be obtained. Using this water permeability in nondeformed conditions, the water flux in the ALFS and ALDS modes can be normalized to indicate how much water flux was reduced in each mode due to CP (Figure 2(c) and 2(d)). For

the PA-TFC membrane, the normalized water flux asymptotically decreases with increasing bulk osmotic pressure. The TS and TS+FS configurations show relatively lower water flux than that of the FS configuration, indicating that a dense tricot spacer (TS) located near the membrane surface increases extent of CP, thus further reducing the effective osmotic pressure. In addition, a feed spacer located in the bulk region does not reduce CP as effectively as the FS configuration when a denser spacer is already located near the membrane surface (TS+FS). This observation corresponds to other studies in which feed spacers in contact with membrane surfaces are more likely to disturb the CP layer and thus enhance mass transfer[20,25,26]. In the ALDS mode, the water flux differences due to the spacer configuration were relatively small compared to those in the ALFS mode, meaning that the importance of spacer selection in reducing CP is more significant in dilutive internal concentration polarization (DICP) and dilutive external concentration polarization (DECP) on the draw side that in concentrative external concentration polarization (CECP) on the feed side.

Deterioration of selectivity of FO membrane due to structural deformation

Generally, nonporous membranes such as FO and RO membranes are assumed to have a unity reflection coefficient ($\sigma = 1$), which means that the membrane is completely selective to solute species in nondeformed conditions. However, as hydraulic pressure engages the deformable membrane structure, it loses its ability as a complete barrier, and accordingly, the effective osmotic pressure decreases. This reduction in selectivity can be quantified by the reflection coefficient (σ) as a function of corresponding osmotic pressure / adjusted hydraulic pressure ($\Delta\pi = \Delta P/\sigma$) in each null-flux mode. Using Equation S11, the reflection coefficient was

derived in null-flux mode to examine the structural vulnerability of the membrane to hydraulic pressure. As shown in Figure 4(a) and 4(b), the CTA-ES2 membrane is highly vulnerable compared to the PA-TFC membrane in terms of a decreasing trend in the reflection coefficient. Membrane compaction (TS) has a much smaller effect on the reduction in the reflection coefficient than membrane stretching (TS+FS and FS) for both membranes. Here, it is intriguing to note that even under identical hydraulic pressure and spacer configurations, each membrane corresponds differently in terms of the reflection coefficient. For example, compared to the FS configuration, the TS+FS configuration exhibits some partial effectiveness in reducing the reduction in the reflection coefficient for PA-TFC (Figure 4(a)) but shows little effect for CTA-ES2. This result suggests that using the TS+FS configuration may not be sufficient to avoid membrane deformation, particularly for the CTA-ES2 membrane.

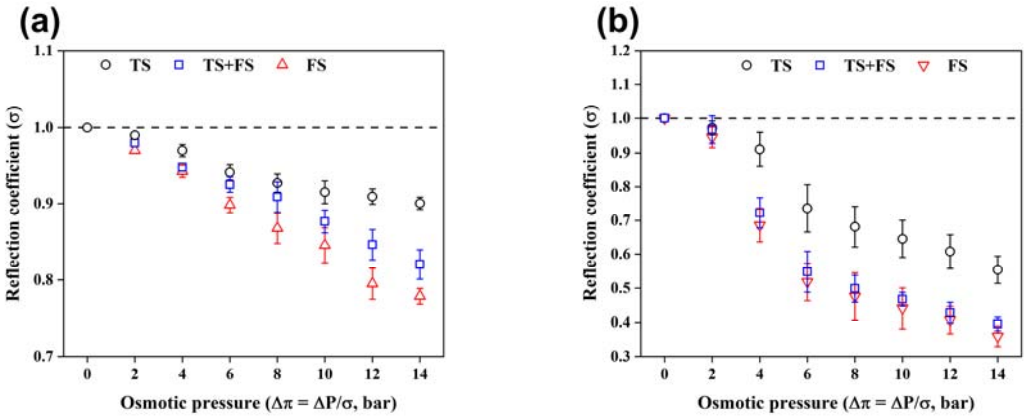

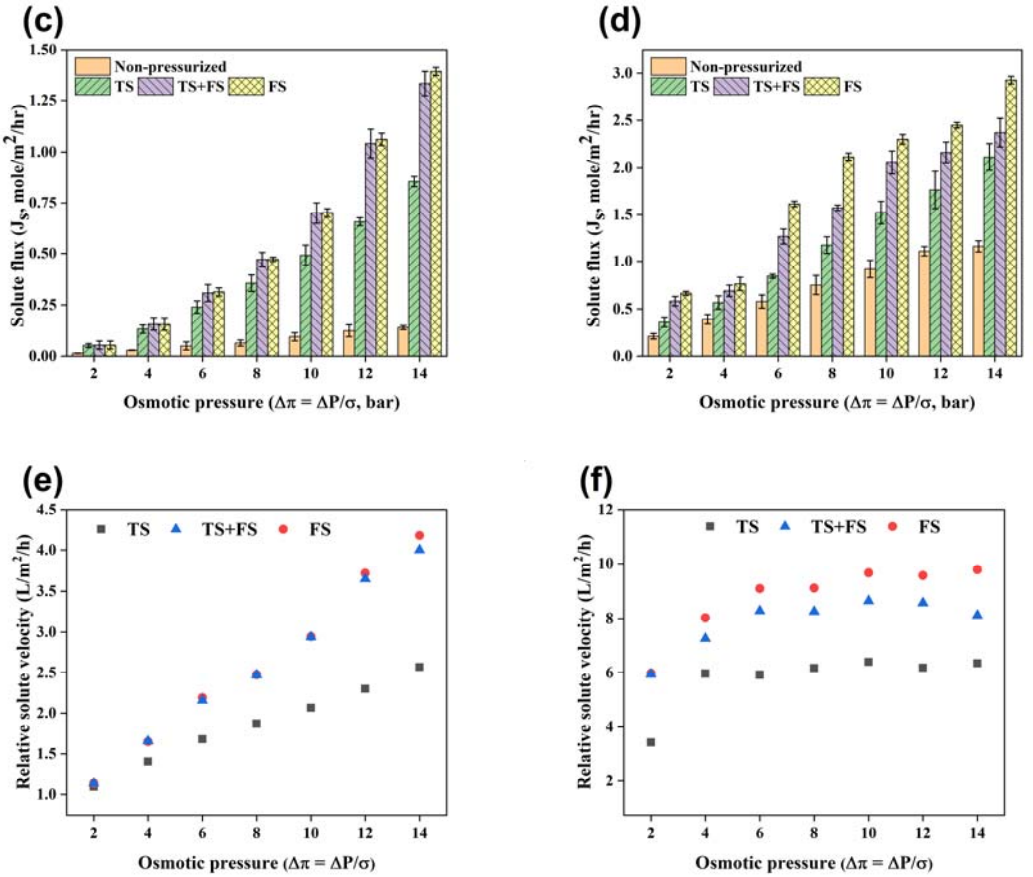

Figure 4. Reduction in the reflection coefficient for three spacer configurations, TS, TS+FS, and FS, for (a) PA-TFC and (b) CTA-ES2. Comparison of solute flux under the nonpressurized ALDS mode and null-flux mode for (c) PA-TFC and (d) CTA-ES2. Relative solute velocity derived by normalizing the solute flux by the respective NaCl concentration for (e) PA-TFC and (f) CTA-ES2. Figure 4(c) and 4(d) compare the solute fluxes under the nonpressurized ALDS mode and null-flux mode for the three spacer configurations.

The CTA-ES2 membrane shows higher solute flux in all operation modes than the PA-TFC membrane. However, the ratio of ~~in~~ the solute flux under pressurized mode (null-flux mode) over that under nonpressurized mode and pressurized mode (null-flux mode) was significantly higher for PA-TFC (approx. 10-fold) than for CTA-ES2 (approx. 2-fold). This increased solute transport under pressurized mode can be explained by two factors: (i) convective solute

transport through defects in the active layer formed by membrane deformation and (ii) enhanced solute diffusion by the higher effective concentration difference under null-flux mode (due to negligible CP under this condition). Based on the observation of different solute fluxes under membrane compaction (TS) and membrane stretching (TS+FS and FS), it is evident that membranes become more permeable to solute species with tensile stretching.

The solute flux increases as a function of the concentration difference across the membrane where there is no water transport ($J_w = 0$)[31]. To remove the concentration dependence, the relative solute velocity was derived by normalizing the solute flux by the corresponding NaCl concentration based on Equation S13 (Figure 4(e) and (f)). The slopes of the plots in these figures show that increasing solute transport is solely based on selectivity deterioration as a function of hydraulic pressure, excluding the effects of CP and NaCl concentration. Thus, this slope can be used as a coefficient of membrane selectivity deterioration due to spacer-induced membrane deformation. The relative solute velocity of the CTA-ES2 membrane showed a significant initial increase up to 6 bar but then leveled off without a significant increase, while that of PA-TFC showed a constant increasing trend. This most likely means that the active layer of CTA-ES2 was already fully stretched (i.e., losing integrity for selectivity) at 6 bar of hydraulic pressure regardless of the spacer configuration, but the active layer of PA-TFC was relatively more flexible to show a constant increasing trend in the given pressure range. Differences between the TS+FS and FS configurations were found above 4 bar for CTA-ES2 and 12 bar for PA-TFC. It should be noted that loose membranes such as CTA-ES2 may not be appropriate for this analysis since they exhibit severe nonlinearity, as shown in Figure 3(f).

Relation between mechanical strength of membrane and structural vulnerability

Mechanical strength of membrane is directly related to the susceptibility of the membrane against spacer-induced membrane deformation, and resulted membrane's permeation characteristics. Several studies[22~24] examined the mechanical strength of PA-TFC and CTA-ES membranes in a dried state, however, the mechanical strength of the membranes in wet-state has not been investigated. Although it is common to use dried specimens for mechanical analysis, the mechanical strength of the wet membrane also needs to be analyzed since FO membrane's permeation characteristics are measured in a wet state. To comparatively examine the mechanical strength of PA-TFC and CTA-ES2 membranes in a dried and wet state, the uniaxial tensile test was conducted. As shown in Table. S1, ultimate tensile strength (UTS) of the PA-TFC membrane was somewhat increased to 66.2±3.18 MPa after wetting in water compared to the dried state (66.6±3.94 MPa), whereas UTS value of the CTA-ES2 membrane was 47.6±0.8 MPa in a dried state, and it was decreased to 44.1±1.2 MPa after wetting in water. The higher UTS value of the wet PA-TFC membrane than that of the dried PA-TFC membrane is not the behavior of typical polymeric materials. This result can be originated from the unique structure of the PA-TFC membrane. Because of the polyester mesh is embedded inside the polysulfone, water molecules can interact as a cross-linker by hydrogen bonding between the polymers when the membrane is wet[28,33-36]. The increased elastic modulus of the wet PA-TFC membrane can also be considered in connection with the phenomenon described above. The elastic modulus of dried and wet PA-TFC membrane was 716.7±57.26 and 736.3±74.87 MPa, respectively. And, the behavior of the membranes was almost same in before and after wetting, which means that water molecules affect the strength of interactions

between materials and structural stability in the region of elastic deformation without changing the intrinsic physical properties of the polymers. The elastic modulus of the dried and wet CTA-ES2 membrane was 824.8±167.47 and 531.8±102.25 MPa, respectively. This is a common result that the mechanical strength is weakened because the structure loosens when the polymer or organic material is wet with water[37,38]. This drastic reduction of mechanical strength and inherent stiffness of CTA-ES2 membrane in wet state explains high susceptibility of CTA-ES2 membrane to hydraulic pressure (i.e. severe reduction of reflection coefficient under pressurization). The evidence of the structural vulnerability of CTA-ES2 membrane can also be found in visual observation. Membrane surfaces before-and-after pressurization analyzed by scanning electron microscopy (SEM) (Figure S2 and S3 for PA-TFC and CTA-ES2 membrane) reveals that CTA-ES2 membrane showed severer structural damages than PA-TFC membrane on both active and support layers more. Furthermore, more visible damages with membrane stretching (FS) than with membrane compaction (TS) for both membranes. Although, PA-TFC membrane turned out to be more vulnerable specifically for membrane stretching by feed spacer on the active layer as it shows evident rupture by feed spacer filament (Figure S2(e)) This can be attributed to structural differences in the active layer and intermediate layer between the active and support layers. Unlike a PA membrane, which is composed of a polysulfone support layer and a thin polyamide active layer bonded by interfacial polymerization (IP), a CTA membrane is composed of a single component, and the active layer is formed by thermal treatment of the support layer. Due to this relatively weak IP-bonded interface compared to the thermally treated interface in a CTA membrane[27], a PA membrane can be more vulnerable to structural deformation of the active layer. In addition, the flexibility of the polyamide active layer[30] allows the solute flux of the PA-TFC membrane to be more varied than that of the CTA-ES2 membrane. In this respect, the PA-TFC membrane

shows a higher solute flux increment ratio (approx. 10 times) between nonpressurized and pressurized conditions than the CTA-ES2 membrane (approx. 2 times), as shown in Figure 4(c) and (d).

The other important aspect of membrane deformation is channel pressure drop due to the contracted channel geometry under pressurized conditions. At present, no method has been developed to quantify this channel contraction and resulted reduction in channel volume. However, this channel contraction can be indirectly estimated by the channel pressure drop measured in deformed channel conditions. As shown in Figure S5, CTA-ES2 membrane revealed a higher channel pressure drop than that of PA-TFC membrane, which can be attributed by the aforementioned drastic reduction of mechanical strength and stiffness of CTA-ES2 membrane in a wet state.

Change in interdependence between water and solute transport

To assess the interdependence between volumetric flux (J_v) and relative solute velocity (J_s), the experimentally obtained reflection coefficient was plotted as a function of the reciprocal coefficient that is derived by reciprocal relations (Equations S6 and S7). Figure 5 depicts this interdependence for the PA-TFC and CTA-ES2 membranes for different spacer configurations. Throughout the given range of the reflection coefficient, membrane compaction (TS) induces a lower reciprocal coefficient than membrane stretching (TS+FS and FS) because membrane stretching makes the membrane more vulnerable to solute transport, as shown in previous results. The FS configuration seems to have a lower reciprocal coefficient than the TS+FS configuration in the low-pressure range but exceeds the TS+FS configuration above 6 bar with

371 a steep increase in this coefficient. This finding is most likely due to the initial difference in
372 water permeability caused by the shadow effect, and the shadow effect is then dominated by
373 the effect of membrane stretching above 6 bar. On the other hand, CTA-ES2 reveals a
374 drastically lower reciprocal coefficient than PA-TFC with a relatively small deviation. As
375 depicted in Figure 5, the reflection coefficient of CTA-ES2 decreases much more rapidly than
376 that of PA-TFC, indicating the different pressure susceptibilities of each membrane. Since a
377 higher negative value of the reciprocal coefficient means more ideal membrane conditions (less
378 interaction between water and solute transport), the CTA-ES2 membrane can be defined as a
379 highly leaky membrane with high pressure vulnerability compared to PA-TFC, which can be
380 defined as a dense membrane.

381

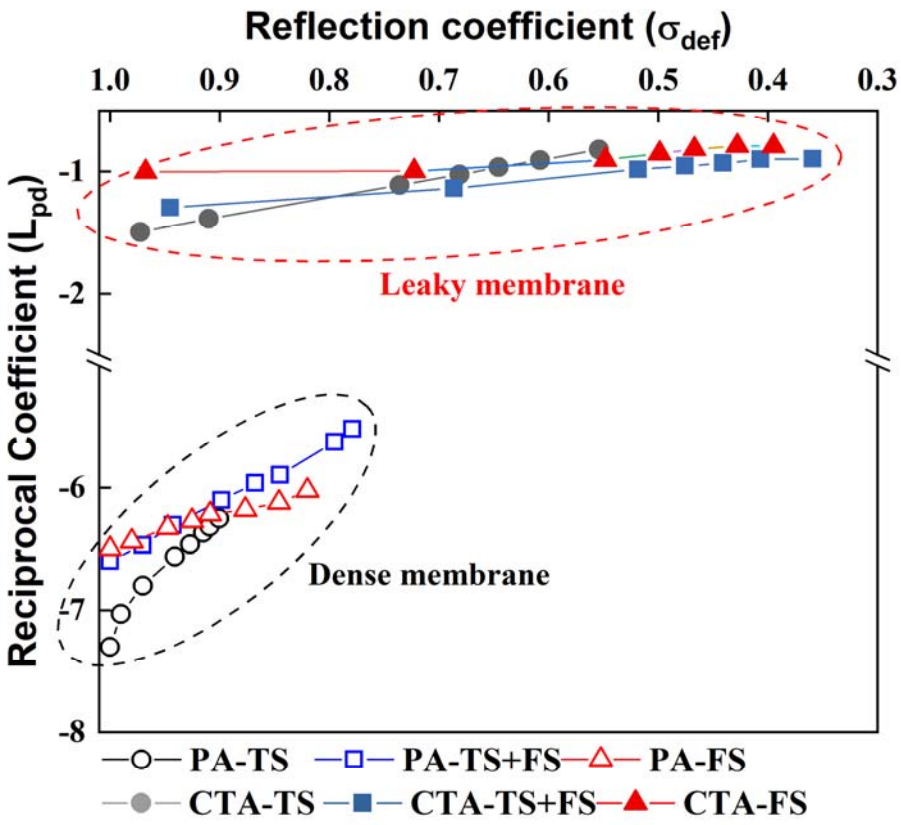

382

383 **Figure 5.** Reciprocal coefficient as a function of the reflection coefficient for PA-TFC and
384 CTA-ES2.

385

386 ## Characteristics of FO membranes: S-D model and irreversible
387 ## thermodynamic model

388 There are several blind spots in general S-D model-based characterization methods as follows:
389 (i) A single permeability coefficient is assumed regardless of spacer and hydraulic pressure
390 conditions; (ii) No interaction between solute and water transport is considered; (iii) A
391 nonporous membrane and only diffusion transport of water and solute are assumed. In the
392 current study, alteration of water and solute permeability was demonstrated under both

pressurized and nonpressurized conditions for three spacer configurations. As demonstrated in the results, alteration of water and solute permeability is significant and varies depending on the spacer configuration in a given hydraulic pressure range. These deviations may be negligible in an RO process since these discrepancies would be insignificant under high operating pressures (40~60 bar) with a single-spacer configuration (i.e., tricot spacer). However, when considering that ODMPs use relatively various spacer configurations under low operating pressures (below 20 bar), this deviation of the permeability coefficients needs to be considered in precisely estimating and analyzing process performance. The interdependence between solute and water transport was quantified by the reciprocal coefficient as a function of the reflection coefficient shown in Figure 5. This unique characterization method based on thermodynamic assessment can provide a new aspect regarding transport mechanisms in membrane processes. However, the literature covering this aspect is severely limited at the moment in terms of discussion, and further experimental validation is required for the validity of this approach.

On the other hand, a drawback of thermodynamic assessment is that it does not provide insights regarding the physical and chemical status of the solution inside and near the membrane, while an S-D model-based method attempts to draw a concentration profile in association with the structural characteristics of the membrane and flow characteristics in the flow channel (i.e., ICP and ECP equations). However, it should not be forgotten that all these theoretical works can only be validated by the resultant volume and concentration changes in solutions during process operation. Furthermore, the structural parameter (S) and mass transfer coefficient (k), which are the most important factors for addressing ICP and ECP, respectively, cannot be experimentally validated. For example, as shown in Equation S5, the structural parameter is

theoretically dependent on the thickness, tortuosity and porosity of the support layer, but in most studies, this S value is derived from predetermined A and B values using Equation S3 due to difficulties in nanoscale measurements of those structural characteristics. The mass transfer coefficient can be derived using the relation given in Equations S6 and S7; however, this approach may not be suitable to precisely resolve a complicated geometry of spacer-filled narrow channel and the resulted complex microflow near the membrane surface.

Effect of spacer configuration on membrane deformation and CP

As discussed in the previous section, it is not viable to draw a concentration profile across the membrane layers solely based on experimentally measured values. However, the cause-specific proportions of the osmotic pressure drop can be derived purely based on phenomenological assessments using three assumptions: (i) In the nonpressurized ALDS mode, the effect of ICP can be neglected (i.e., the core assumption in nonpressurized characterization methods for FO membranes[32]); (ii) The nondeformed water permeability derived by empirical relation (Figure 3) can be postulated as water permeability excluding the effects of membrane deformation and CP; iii) The Staverman reflection coefficient measured under null-flux mode represents the osmotic pressure drop solely by membrane deformation. Although the effects of deformation and CP cannot be directly compared due to differences in their mechanisms, the proportions of the osmotic pressure drop by CP and deformation can be compared as a function of the same extent of osmotic pressure and hydraulic pressure differences. Figure 6(a) and (b) compares the proportion of osmotic pressure drop caused by CP and membrane deformation depending on spacer configuration. The increment ratio of CP-induced osmotic pressure drop by different spacer configurations varied from 7.98% to 20.7% for PA-TFC membrane and from 0.19% to 4.76% for CTA-ES2 membrane. Theoretically, CP is the resultant of the membrane's

equilibrium in association with water and solute transports, yet mostly due to water transport[39]. In this respect, the difference in the increment ratio is attributed to the different water permeability of the two membranes (~5-fold difference). On the other hand, the deformation-induced proportion of osmotic pressure drop by spacer configuration increased from 72.3% to 200% and 18.2% ~ 201% for PA-TFC and CTA-ES2 membrane respectively. This difference in variation of osmotic pressure drop is due to different forms and extent of membrane deformation and its susceptibility of each membrane as discussed in previous sections. Overall, the above comparison of osmotic pressure drop caused by CP and membrane deformation reveals the influence of spacer is much greater in membrane deformation than that in CP.

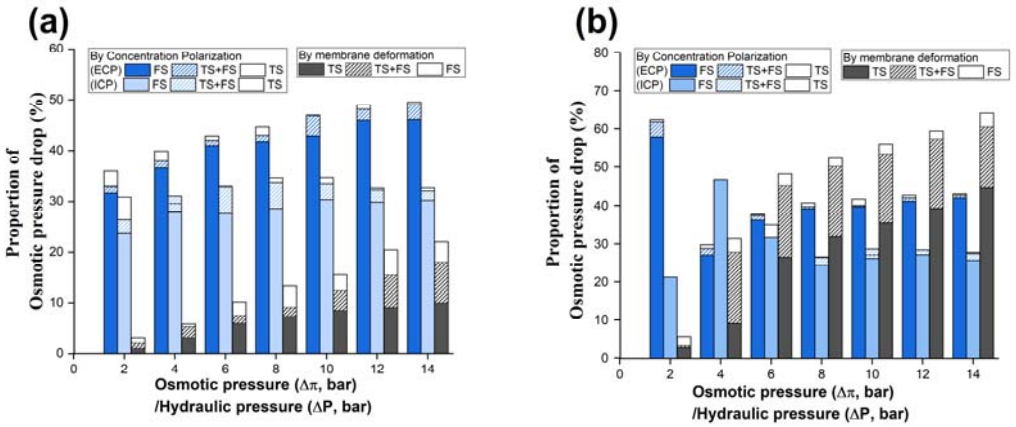

Figure 6. Comparison of proportions of osmotic pressure drop by CP and membrane deformation (PA-TFC for (a) and CTA-ES2 for (b)).

Implications

Membrane deformation and CP are the most dominant factors that reduce effective osmotic pressure in ODMPs. Although these two factors are mutually dependent when hydraulic pressure and osmotic pressure coexist, which is an inevitable circumstance in module-scale operation, the two factors were differentiated and comparatively quantified using extensive theoretical and experimental analyses for a deeper understanding of the permeation characteristics of FO membranes. It was demonstrated that membrane deformation, especially membrane stretching and the resulting selectivity loss, can be controlled by a combined configuration with a feed spacer and tricot spacer. The results also revealed that the role of a spacer in reducing deformation-induced osmotic pressure drop is more significant than that in reducing CP-induced osmotic pressure drop under identical osmotic and hydraulic pressures. Although most spacer research has tended to focus on enhancing mass transfer by reducing CP, the results in this study imply that mitigation of membrane deformation and the resulted deterioration of process performance need to be considered more in membrane and spacer studies. The membrane characterization method suggested in this study can be utilized to quantitatively and differentially evaluate the effects of membrane deformation and CP on effective osmotic pressure drop for the development of ODMP membranes and spacers.

Although the current study focuses primarily on the effect of spacer configuration on membrane deformation and CP, spacer also have major effect on fouling. For example, spacer geometry can directly affect the fluid dynamics of spacer-filled channels to mitigate foulant deposition[40]. However, in the context of ODMPs, severe spacer-induced deformation may block the flow channels and result in severe membrane fouling. In addition, the increased reverse solute diffusion (e.g., of fouling precursors such as Ca^{2+})[41] as a result of severe

membrane deformation can accelerate fouling and scaling[42,43]. Future studies need to systematically investigate these competing effects of spacers on fouling of ODMP membranes.

Supporting Information

SEM images of cross-section and surface of PA-TFC and CTA-ES2 membrane before and after pressurization, images of feed spacer and tricot spacer, mechanical properties of PA-TFC and CTA-ES2 membrane in dried and wet state, detailed experimental set-up for pressurized and nonpressurized tests, experimental results on channel pressure drop, and theoretical backgrounds regarding FO membrane characterization with the effect of the spacer.

Acknowledgement

This work was supported by Korea Environment Industry & Technology Institute (KEITI) through Industrial Facilities & Infrastructure Research Program, funded by Korea Ministry of Environment (MOE) (1485016290)

References

(1) Akther, N.; Sodiq, A.; Giwa, A.; Daer, S.; Arafat, H. A.; Hasan, S. W. Recent Advancements in Forward Osmosis Desalination: A Review. Chem. Eng. J. 2015, 281, 502–522. https://doi.org/10.1016/j.cej.2015.05.080.

(2) Altaee, A.; Sharif, A. Pressure Retarded Osmosis: Advancement in the Process Applications for Power Generation and Desalination. Desalination 2015, 356, 31–46. https://doi.org/10.1016/j.desal.2014.09.028.

(3) Attarde, D.; Jain, M.; Singh, P. K.; Gupta, S. K. Energy-Efficient Seawater Desalination and

Wastewater Treatment Using Osmotically Driven Membrane Processes. Desalination 2017, 413, 86–100. https://doi.org/10.1016/j.desal.2017.03.010.

(4) Lutchmiah, K.; Verliefde, A. R. D.; Roest, K.; Rietveld, L. C.; Cornelissen, E. R. Forward Osmosis for Application in Wastewater Treatment: A Review. Water Res. 2014, 58 (0), 179–197. https://doi.org/10.1016/j.watres.2014.03.045.

(5) Tang, C. Y.; She, Q.; Lay, W. C. L.; Wang, R.; Fane, A. G. Coupled Effects of Internal Concentration Polarization and Fouling on Flux Behavior of Forward Osmosis Membranes during Humic Acid Filtration. J. Memb. Sci. 2010, 354 (1–2), 123–133. https://doi.org/10.1016/j.memsci.2010.02.059.

(6) Phuntsho, S.; Hong, S.; Elimelech, M.; Shon, H. K. Osmotic Equilibrium in the Forward Osmosis Process: Modelling, Experiments and Implications for Process Performance. J. Memb. Sci. 2014, 453, 240–252. https://doi.org/10.1016/j.memsci.2013.11.009.

(7) Phillip, W. A.; Yong, J. S.; Elimelech, M. Reverse Draw Solute Permeation in Forward Osmosis: Modeling and Experiments. Environ. Sci. Technol. 2010, 44 (13), 5170–5176. https://doi.org/10.1021/es100901n.

(8) Choi, B. G.; Zhan, M.; Shin, K.; Lee, S.; Hong, S. Pilot-Scale Evaluation of FO-RO Osmotic Dilution Process for Treating Wastewater from Coal-Fired Power Plant Integrated with Seawater Desalination. J. Memb. Sci. 2017, 540 (May), 78–87. https://doi.org/10.1016/j.memsci.2017.06.036.

(9) Kim, J.; Blandin, G.; Phuntsho, S.; Verliefde, A.; Le-Clech, P.; Shon, H. Practical Considerations for Operability of an 8″ Spiral Wound Forward Osmosis Module: Hydrodynamics, Fouling Behaviour and Cleaning Strategy. Desalination 2017, 404, 249–258. https://doi.org/10.1016/j.desal.2016.11.004.

(10) Im, S. J.; Jeong, S.; Jang, A. Feasibility Evaluation of Element Scale Forward Osmosis for Direct Connection with Reverse Osmosis. J. Memb. Sci. 2018, 549 (September 2017), 366–376. https://doi.org/10.1016/j.memsci.2017.12.027.

(11) Lee, E. S. H.; Xiong, J. Y.; Han, G.; Wan, C. F.; Chong, Q. Y.; Chung, T. S. A Pilot Study on Pressure Retarded Osmosis Operation and Effective Cleaning Strategies. Desalination 2017, 420 (August), 273–282. https://doi.org/10.1016/j.desal.2017.08.004.

(12) Kook, S.; Lee, C.; Nguyen, T. T.; Lee, J.; Shon, H. K.; Kim, I. S. Serially Connected Forward Osmosis Membrane Elements of Pressure-Assisted Forward Osmosis-Reverse Osmosis Hybrid System: Process Performance and Economic Analysis. Desalination 2018, 448 (September), 1–12. https://doi.org/10.1016/j.desal.2018.09.019.

(13) Kim, Y. C.; Elimelech, M. Adverse Impact of Feed Channel Spacers on the Performance of Pressure Retarded Osmosis. Environ. Sci. Technol. 2012, 46 (8), 4673–4681. https://doi.org/10.1021/es3002597.

(14) Xie, M.; Tang, C. Y.; Gray, S. R. Spacer-Induced Forward Osmosis Membrane Integrity Loss during Gypsum Scaling. Desalination 2016, 392, 85–90. https://doi.org/10.1016/j.desal.2016.04.017.

(15) She, Q.; Hou, D.; Liu, J.; Tan, K. H.; Tang, C. Y. Effect of Feed Spacer Induced Membrane Deformation on the Performance of Pressure Retarded Osmosis (PRO): Implications for PRO Process Operation. J. Memb. Sci. 2013, 445, 170–182. https://doi.org/10.1016/j.memsci.2013.05.061.

(16) Muhammad Alvan Hidayat, Kook, S.; Kim, I. S. Draw Channel Contraction of an 8040 Spiral-Wound Forward Osmosis Membrane Element in Pressure-Assisted Forward Osmosis (PAFO). Desalin. Water Treat. 2018, 109, 17–27. https://doi.org/10.5004/dwt.2018.22152.

(17) Kim, J. E.; Phuntsho, S.; Ali, S. M.; Choi, J. Y.; Shon, H. K. Forward Osmosis Membrane Modular Configurations for Osmotic Dilution of Seawater by Forward Osmosis and Reverse Osmosis Hybrid System. Water Res. 2018, 128, 183–192. https://doi.org/10.1016/j.watres.2017.10.042.

(18) Kim, Y. C.; Kim, Y.; Oh, D.; Lee, K. H. Experimental Investigation of a Spiral-Wound Pressure-Retarded Osmosis Membrane Module for Osmotic Power Generation. Environ. Sci. Technol. 2013, 47 (6), 2966–2973. https://doi.org/10.1021/es304060d.

(19) McCutcheon, J. R.; McGinnis, R. L.; Elimelech, M. Desalination by Ammonia-Carbon Dioxide Forward Osmosis: Influence of Draw and Feed Solution Concentrations on Process Performance. J. Memb. Sci. 2006, 278 (1–2), 114–123. https://doi.org/10.1016/j.memsci.2005.10.048.

(20) Zhang, H.; Cheng, S.; Yang, F. Use of a Spacer to Mitigate Concentration Polarization during Forward Osmosis Process. Desalination 2014, 347, 112–119. https://doi.org/10.1016/j.desal.2014.05.026.

(21) Lee, K. L.; Baker, R. W.; Lonsdale, H. K. Membranes for Power Generation by Pressure-Retarded Osmosis. J. Memb. Sci. 1981, 8 (2), 141–171. https://doi.org/10.1016/S0376-7388(00)82088-8.

(22) Kim, B.; Gwak, G.; Hong, S. Review on Methodology for Determining Forward Osmosis (FO) Membrane Characteristics: Water Permeability (A), Solute Permeability (B), and Structural Parameter (S). Desalination 2017, 422 (February), 5–16. https://doi.org/10.1016/j.desal.2017.08.006.

(23) Kook, S.; Swetha, C. D.; Lee, J.; Lee, C.; Fane, T.; Kim, I. S. Forward Osmosis Membranes under Null-Pressure Condition: Do Hydraulic and Osmotic Pressures Have Identical Nature? Environ. Sci. Technol. 2018, 52 (6), 3556–3566. https://doi.org/10.1021/acs.est.7b05265.

(24) Kim, S. J.; Kook, S.; O'Rourke, B. E.; Lee, J.; Hwang, M.; Kobayashi, Y.; Suzuki, R.; Kim, I. S. Characterization of Pore Size Distribution (PSD) in Cellulose Triacetate (CTA) and Polyamide (PA) Thin Active Layers by Positron Annihilation Lifetime Spectroscopy (PALS) and Fractional Rejection (FR) Method. J. Memb. Sci. 2017, 527 (June 2016), 143–151. https://doi.org/10.1016/j.memsci.2016.12.064.

(25) Park, M.; Kim, J. H. Numerical Analysis of Spacer Impacts on Forward Osmosis Membrane Process Using Concentration Polarization Index. J. Memb. Sci. 2013, 427, 10–20. https://doi.org/10.1016/j.memsci.2012.09.045.

(26) Wang, Y.; Zhang, M.; Liu, Y.; Xiao, Q.; Xu, S. Quantitative Evaluation of Concentration Polarization under Different Operating Conditions for Forward Osmosis Process. Desalination 2016, 398, 106–113. https://doi.org/10.1016/j.desal.2016.07.015.

(27) Hayashi, M.; Hashimoto, T.; Hasegawa, H.; Takenaka, M.; Grüll, H.; Esker, A. R.; Weber, M.; Satija, S. K.; Han, C. C.; Nagao, M. Interface between a Polysulfone and Polyamide as Studied by Combined Neutron Reflectivity and Small-Angle Neutron Scattering Techniques. Macromolecules 2000, 33 (22), 8375–8387. https://doi.org/10.1021/ma000661g.

(28) Hosaka, K.; Tagami, J.; Nishitani, Y.; Yoshiyama, M.; Carrilho, M.; Tay, F. R.; Agee, K. A.; Pashley, D. H. Effect of Wet vs. Dried Testing on the Mechanical strength of Hydrophilic Self-Etching Primer Polymers. Eur. J. Oral Sci. 2007, 115 (3), 239–245. https://doi.org/10.1111/j.1600-0722.2007.00452.x.

(29) Oh, Y.; Lee, S.; Elimelech, M.; Lee, S.; Hong, S. Effect of Hydraulic Pressure and Membrane

577 Orientation on Water Flux and Reverse Solute Flux in Pressure Assisted Osmosis. J. Memb. Sci. 2014,
578 465, 159–166. https://doi.org/10.1016/j.memsci.2014.04.008.

579 (30) Reglero Ruiz, J. A.; Trigo-López, M.; García, F. C.; García, J. M. Functional Aromatic Polyamides.
580 Polymers (Basel). 2017, 9 (9), 414. https://doi.org/10.3390/polym9090414.

581 (31) Kedem, O.; Katchalsky, A. Thermodynamic Analysis of the Permeability of Biological Membranes to
582 Non-Electrolytes. Biochim. Biophys. Acta 1958, 27, 229–246. https://doi.org/10.1016/0006-
583 3002(58)90330-5.

584 (32) B. Kim, G. Gwak, S. Hong, Review on methodology for determining forward osmosis (FO) membrane
585 characteristics: Water permeability (A), solute permeability (B), and structural parameter (S),
586 Desalination. 422 (2017) 5–16. doi:10.1016/j.desal.2017.08.006.

587 (33) ASTM D638-14, Standard Test Method for Tensile Properties of Plastics, ASTM International, West
588 Conshohocken, PA, 2014, www.astm.org

589 (34) Han, F.; Zhang, H.; Zhao, J.; Zhao, Y.; Yuan, X. Diverse Release Behaviors of Water-Soluble Bioactive
590 Substances from Fibrous Membranes Prepared by Emulsion and Suspension Electrospinning. J. Biomater.
591 Sci. Polym. Ed. 2013, 24 (10), 1244–1259. https://doi.org/10.1080/09205063.2012.746510.

592 (35) Hou, H.; Wang, S.; Jin, W.; Jiang, Q.; Sun, L.; Jiang, L.; Sun, G. KOH Modified Nafion112 Membrane for
593 High Performance Alkaline Direct Ethanol Fuel Cell. Int. J. Hydrogen Energ. 2011, 36 (8), 5104–5109.
594 https://doi.org/10.1016/j.ijhydene.2010.12.093.

595 (36) Lee, K. H.; Kim, H. Y.; Ryu, Y. J.; Kim, K. W.; Choi, S. W. Mechanical Behavior of Electrospun Fiber
596 Mats of Poly(Vinyl Chloride)/Polyurethane Polyblends. J. Polym. Sci. B Polym. Phys. 2003, 41 (11),
597 1256–1262. https://doi.org/10.1002/polb.10482.

598 (37) Qasim, S. B.; Delaine-Smith, R. M.; Fey, T.; Rawlinson, A.; Rehman, I. U. Freeze Gelated Porous
599 Membranes for Periodontal Tissue Regeneration. Acta Biomater. 2015, 23, 317–328.
600 https://doi.org/10.1016/j.actbio.2015.05.001.

601 (38) Yagoub, H.; Zhu, L.; Shibraen, M. H. M. A.; Xu, X.; Babiker, D. M. D.; Xu, J.; Yang, S. Complex

Membrane of Cellulose and Chitin Nanocrystals with Cationic Guar Gum for Oil/Water Separation. J. Appl. Polym. Sci. 2019, 136 (37), 47947. https://doi.org/10.1002/app.47947.

(39) Tiraferri, A.; Yip, N. Y.; Phillip, W. A.; Schiffman, J. D.; Elimelech, M. Relating Performance of Thin-Film Composite Forward Osmosis Membranes to Support Layer Formation and Structure. J. Memb. Sci. 2011, 367 (1–2), 340–352. https://doi.org/10.1016/j.memsci.2010.11.014.

(40) Abid, H. S.; Johnson, D. J.; Hashaikeh, R.; Hilal, N. A Review of Efforts to Reduce Membrane Fouling by Control of Feed Spacer Characteristics. Desalination 2017, 420 (July), 384–402. https://doi.org/10.1016/j.desal.2017.07.019.

(41) She, Q.; Jin, X.; Li, Q.; Tang, C. Y. Relating Reverse and Forward Solute Diffusion to Membrane Fouling in Osmotically Driven Membrane Processes. Water Res. 2012, 46 (7), 2478–2486. https://doi.org/10.1016/j.watres.2012.02.024.

(42) Zhang, M.; Hou, D.; She, Q.; Tang, C. Y. Gypsum Scaling in Pressure Retarded Osmosis: Experiments, Mechanisms and Implications. Water Res. 2014, 48 (1), 387–395. https://doi.org/10.1016/j.watres.2013.09.051.

(43) Zhang, M.; She, Q.; Yan, X.; Tang, C. Y. Effect of Reverse Solute Diffusion on Scaling in Forward Osmosis: A New Control Strategy by Tailoring Draw Solution Chemistry. Desalination 2017, 401, 230–237. https://doi.org/10.1016/j.desal.2016.08.014.

(44) Kook, S.; Lee, C.; Nguyen, T. T.; Lee, J.; Shon, H. K.; Kim, I. S. Serially Connected Forward Osmosis Membrane Elements of Pressure-Assisted Forward Osmosis-Reverse Osmosis Hybrid System: Process Performance and Economic Analysis. Desalination 2018, 448 (September), 1–12. https://doi.org/10.1016/j.desal.2018.09.019.

(45) Kim, J.; Blandin, G.; Phuntsho, S.; Verliefde, A.; Le-Clech, P.; Shon, H. Practical Considerations for Operability of an 8″ Spiral Wound Forward Osmosis Module: Hydrodynamics, Fouling Behaviour and Cleaning Strategy. Desalination 2017, 404, 249–258. https://doi.org/10.1016/j.desal.2016.11.004.

(46) Schwinge, J.; Wiley, D. E.; Fletcherb, D. F. A CFD Study of Unsteady Flow in Narrow Spacer-Filled Channels for Spiral-Wound Membrane Modules. Desalination 2002, 146 (2002), 195–201.

628

629

Supporting information

Effect of spacer configuration on characteristics of FO membrane: Alteration of permeation characteristics by membrane deformation and concentration polarization

Chulmin Lee[a], Jaewon Jang[a], Nguyen Thanh Tin[a], Suhun Kim[a],Chuyang Y. Tang[b,c,d], In S Kim[a]

a School of Earth Sciences and Environmental Engineering, Gwangju Institute of Science and Technology (GIST), 123 Cheomdangwagi-ro, Buk-gu, Gwangju 61005, South Korea

b Department of Civil Engineering, the University of Hong Kong, Pokfulam, Hong Kong

c UNESCO Centre for Membrane Science and Technology, School of Chemical 9 Engineering, University of New South Wales, Sydney, New South Wales 2052, 10 Australia 11

d UNSW Water Research Centre, School of Civil and Environmental Engineering, 12 University of New South Wales, Sydney, New South Wales 2052, Australia

Corresponding author: +82-62-715-2436, iskim@gist.ac.kr

Pages : 18

Figures : 5

Tables : 1

Table of contents

Membrane and spacer properties

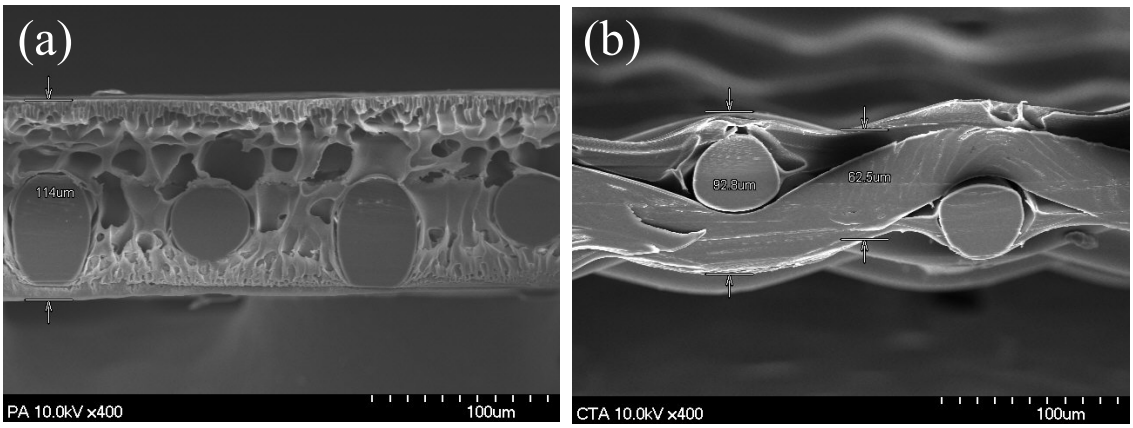

Figure S1. SEM images of cross-section of pristine PA-TFC (a) and CTA-ES2 (b) membrane

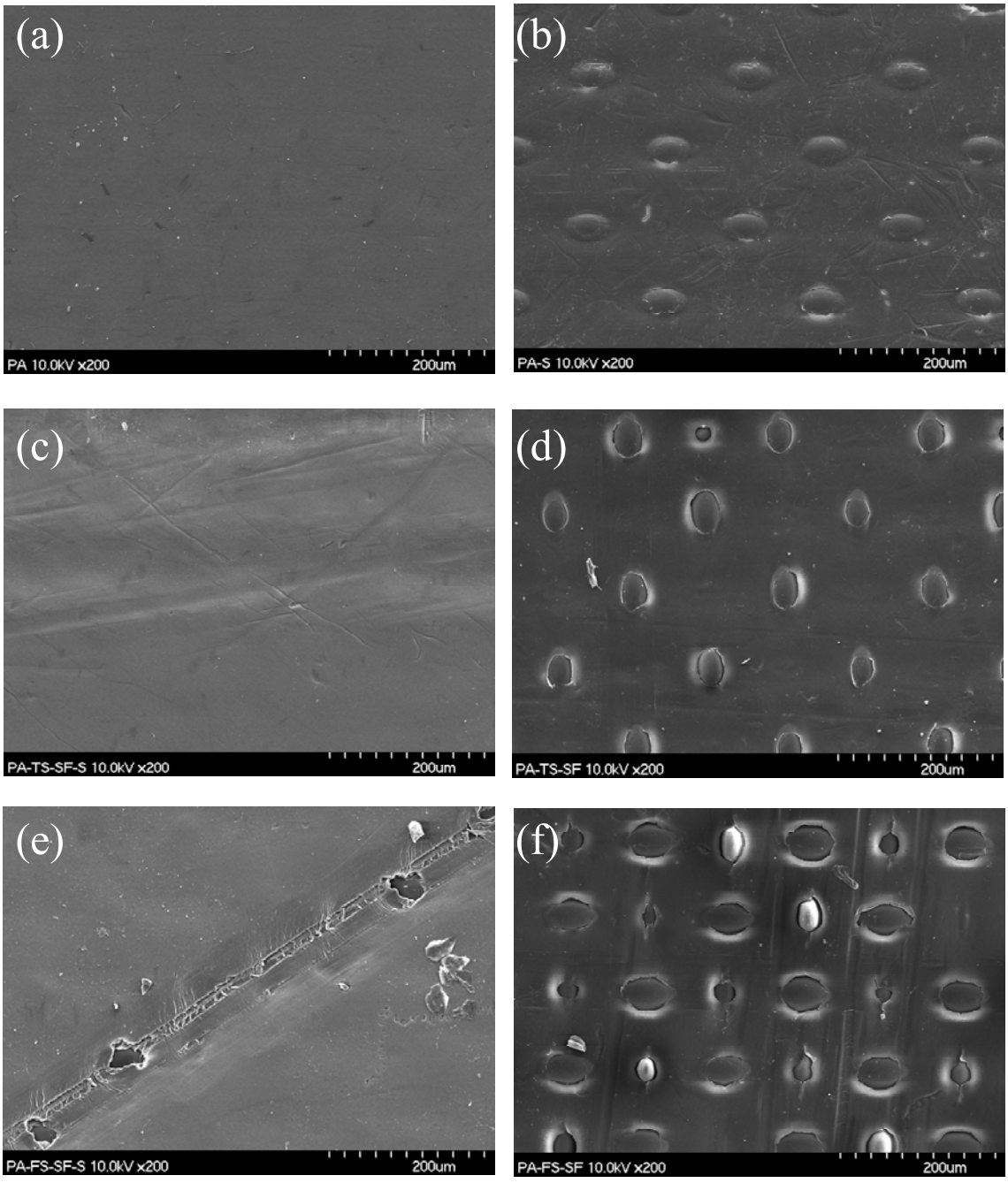

Figure S2. SEM images of active (a, c and e) and support (b, d and f) layer surfaces (PA-TFC membrane): before pressurization (a and b), after pressurization using tricot spacer (TS) (c and d) and feed spacer (FS) (e and f).

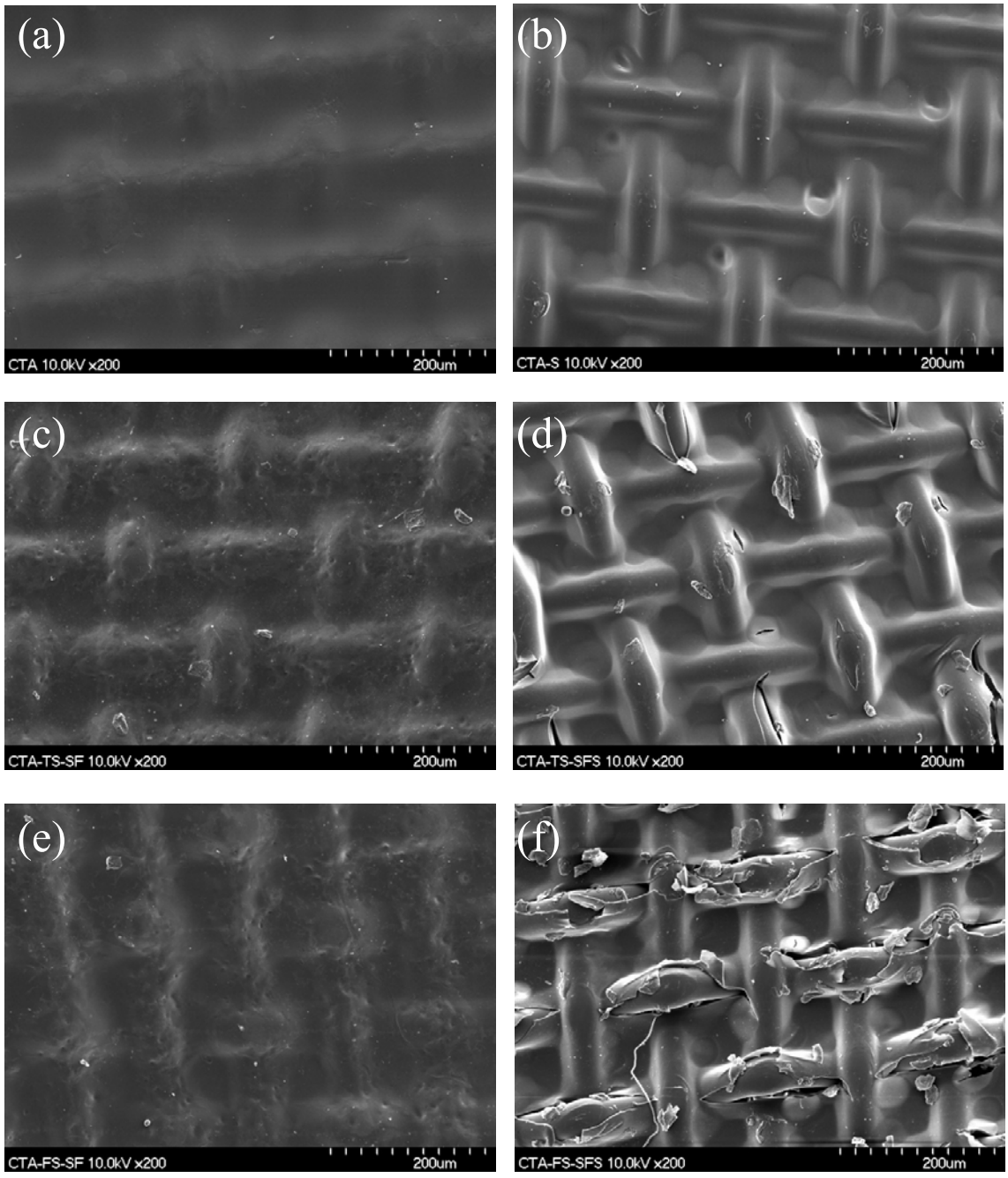

Figure S3. SEM images of active (a, c and e) and support (b, d and f) layer surface (CTA-ES2 membrane): before pressurization (a and b), after pressurization using tricot spacer (TS) (c and d) and feed spacer (FS) (e and f).

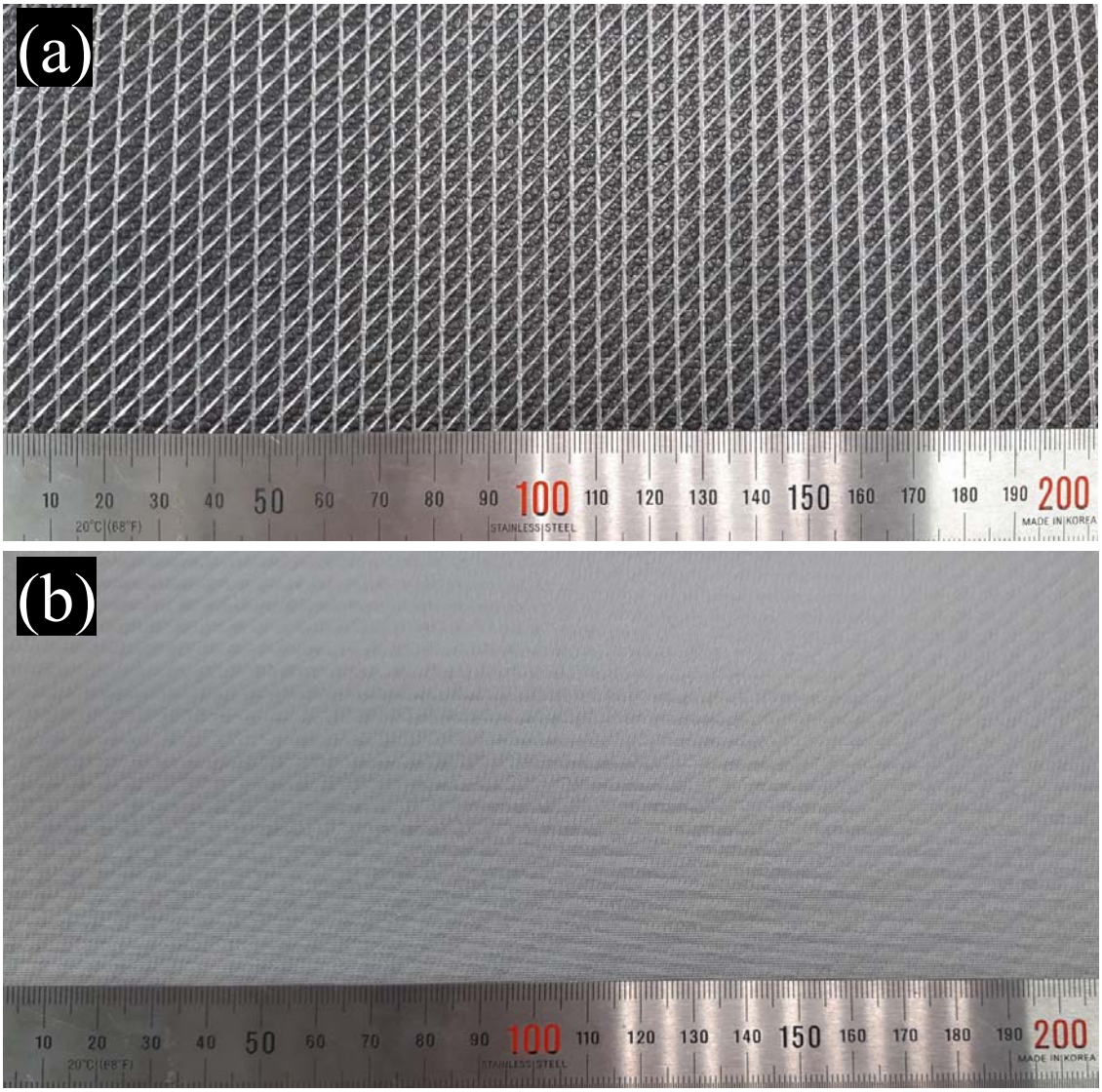

Figure S4. Images of feed spacer (a) and tricot spacer (b)

Table S1. Mechanical properties of PA-TFC and CTA-ES2 membrane in dried and wet state

Properties	PA-TFC		CTA-ES2	
	Dry state	Wet state	Dry state	Wet state
Ultimate tensile strength (UTS, MPa)	66.2±3.18	66.6±3.94	47.6±0.8	44.1±1.2
Elastic modulus (MPa)	716.7±57.26	736.3±74.87	824.8±167.47	531.8±102.25
Elongation at break (%)	15.4±1	14.6±0.275	12.1±0.78	11.4±1.33

Experimental setup

The cross-flow FO experimental setup used in this study is identical to the one described in our previous studies[9-11]. An acryl membrane cell is consisted of two flow channels separated by membrane with dimensions of 2.5 cm (W) x 7.5 cm (L) x 0.3 cm (H) that yield effective membrane area of 18.75 cm^2. Pressure gauges with precision of ± 0.0005 bar precision were installed at the inlet and outlet of the feed and draw channel in order to measure and monitor pressure drop across the feed and draw channels. The effective applied pressure (ΔP) was postulated as the average between inlet and outlet pressure of each channel. The draw solutions were made using NaCl (99.7 % purity, OCI, Korea) as concentrations of 0.0476, 0.0952, 0.1428, 0.1904, 0.238, 0.2856 and 0.3332 M which are equivalent to osmotic pressures of 2 ~ 14 bars at 2 bar interval. A conductivity meter was set in the feed solution to monitor concentration change by the water presence and the reverse solute flux. Water volume of all the solutions are fixed as 2 L and an electronic mass balance (GF-6100, A&D Company, Japan) was used to record the variation in the

175 water mass to enable the calculation of the water flux. Each solution was circulated with
176 constant flowrate of 300 ml/min (i.e. 6.66 cm/s in cross flow velocity) using the pump
177 drive (EW-75211-10, Cole-Parmer, USA) fitted with a magnetic pump head (GB-
178 P25.JVS.A.B1, Micropump, USA). To pressurize the feed solution, a magnetic pump drive
179 (EW-75211-10, Cole-Parmer, USA) coupled with a magnetic pump head (GAF-T23-
180 DEMSE, Micropump, USA) was employed to generate hydraulic pressures ranging from
181 2 to 14 bar at 2 bar interval.

182

Channel pressure drop

Channel pressure drop was obtained by using difference between inlet and outlet pressure of draw flow channel filled with different spacer configurations. Since it is not viable to visually observe actual membrane deformation under hydraulic pressure (Even if visual observation is possible reduced channel volume and geometry cannot be quantified experimentally) during operation this channel pressure drop can provide useful insights as it can be indirect indicator of membrane deformation. Figure S3 (a) and (b) illustrates channel pressure drop depending on spacer configuration as a function of applied hydraulic pressure. In both membranes, TS+FS and FS reveal steep increase compared to gradual increase of TS due to membrane stretching. In TS configuration, structural characteristics of membrane does not seem affect pressure drop as both membranes show almost identical pressure drop. However, extent of pressure drops by membrane stretching turned out to be membrane specific. To examine this difference between two membranes, Hydraulic pressure point was marked where pressure drop of TS+FS and FS exceed that of TS. In PA-TFC, 4.5 and 8.241 bar of pressure drop were required for TS+FS and FS respectively to match identical level of pressure drop of TS while CTA-ES2 membrane demand 2.186 and 4.744 that is approximately half of hydraulic pressure of PA-TFC. To identify ratio of pressure, drop change, in Figure S3 (c) and (d), pressure drop was normalized with the pressure drop under non-pressurized condition. While TS shows almost identical ratio of pressure drop change, steep increase of normalized pressure was identified in both membranes. PA-TFC reveals slightly lower ratio compared to CTA-ES2 membrane with smaller deviation between TS+FS and FS.

205

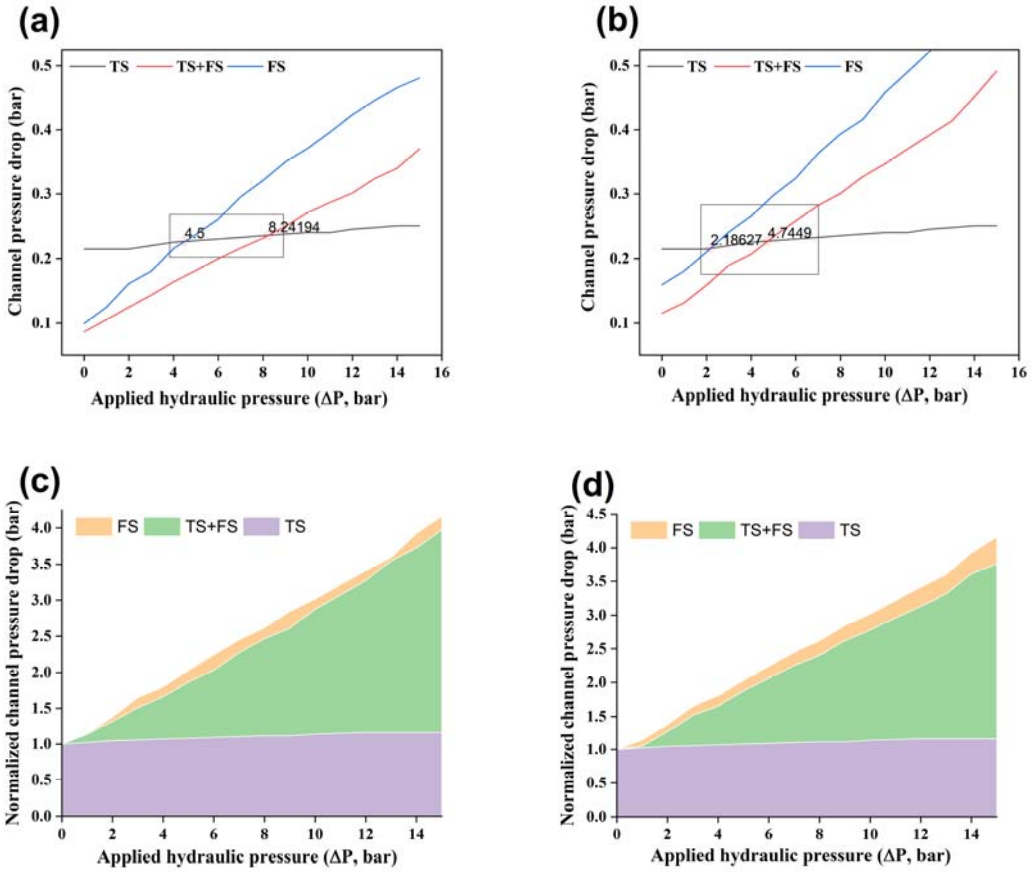

206

207 Figure S5. Channel pressure drop and normalized channel pressure drop of flow channels filled
208 with different spacer configurations for (a), (c) PA-TFC and (b), (d) CTA-ES2

209

Theoretical backgrounds

Characterization of FO membrane associated with effect of spacer

Since early 2000's there have been numerous research efforts to set universal criteria for FO membrane performance along with elucidating permeation mechanism of ODMPs. Since there is no commercialized membrane specifically made for other ODMPs (i.e. PRO and PAFO) at the current stage this FO membrane and module are commonly used for all ODMPs. For characterization of FO membranes, three membrane performance parameters are commonly used based on conventional S-D model: Water permeability, solute permeability and structural parameter, so called A, B and S values[1]. These apparent A, B and S values are determined by various experimental methods and theoretical approaches.

Unlike pressure-driven processes where effect of pressure is dominant and pronounced, ODMPs have more sensitive and complex permeation mechanism that creates many discrepancies in measured performance parameters among FO membrane studies. These discrepancies are mainly attributed to two factors: (1) concentration polarization (CP) (2) membrane deformation. While Internal Concentration Polarization (ICP) is normally considered to be not affected by hydrodynamic condition several experimental studies showed extent of ICP can be altered with External Concentration Polarization (ECP) by spacer configuration and cross-flow velocity[2,3]. To take into account ICP and ECP effect, many theoretical models [4,5] have been suggested based on mass balance across the membrane layers and mass transfer coefficient of flow channel (i.e. one dimensional lump parameter derived from empirical correlation between dimensionless numbers)[6].

The other factor causing discrepancy among literatures is that conventional characterization

method utilizes pressurized condition while ODMPs are operated either under non-pressurized condition or pressure does not act as a main driving force in processes. For this reason, non-pressurized methods for FO membrane was suggested, postulating that ICP can be minimized when active layer of membrane faces draw side[7,8]. These new methods seem to be relatively well accepted in FO community by virtue of better rationale, however, these methods have inherent limitation as it is not able to resolve effect of spacer-induced membrane deformation.

In efforts to further elucidate characteristics of FO membrane in association with structural deformation, novel characterization method for FO membrane was introduced based on irreversible thermodynamics and reciprocal relations of hydraulic and osmotic pressures[9]. Since irreversible thermodynamic model regards membrane as a black box mass transport through membrane is determined by four phenomenological coefficients without consideration of membrane's structural characteristics. However, this approach can provide interesting insight in regard to membrane's structural vulnerability towards external stress created by hydraulic pressure and supporting spacer. More particularly, deterioration of membrane's selectivity and resultant change of interdependence between water and solute transports can be quantified as a function of hydraulic pressure.

Solution-diffusion model

General flux equations for water flux (J_w) and solute flux (J_s) based on conventional S-D model can be expressed as below:

$$J_w = A(\Delta P - \Delta\pi) \quad \text{(S1)}$$

$$J_s = B \cdot \Delta\pi \quad \text{(S2)}$$

Where A and B are water and solute permeability coefficient, ΔP and $\Delta\pi$ are hydraulic and osmotic pressure differences respectively.

Here, ΔP is approximately zero in FO, negative in PRO and positive in PAFO. The driving force for solute flux through the selective layer is concentration difference across it, proportional to $\Delta\pi$.

Based on general flux equations, below equations can be derived with account of internal concentration polarization (ICP) and external concentration polarization (ECP) in associated with membrane structural properties and hydrodynamics near membrane surfaces[7]:

$$J_w = A\left[\frac{\pi_D exp\left(-\frac{J_w S}{D}\right) - \pi_F exp\left(-\frac{J_w}{k}\right)}{1 + \frac{B}{J_w}\left[\exp(\frac{J_w}{k}) - exp(\frac{J_w S}{D})\right]}\right] \quad \text{(S3)}$$

$$J_s = B\left[\frac{C_D exp\left(-\frac{J_w S}{D}\right) - C_F exp\left(\frac{J_w}{k}\right)}{1 + \frac{B}{J_w}\left[exp(\frac{J_w}{k}) - exp(-\frac{J_w S}{D})\right]}\right] \quad \text{(S4)}$$

Where C_D, C_F are bulk concentrations and π_D and π_F are corresponding osmotic pressure on the draw and feed side respectively. k is the solute mass transfer coefficient and D is the

bulk diffusion coefficient of the draw salt.

In eqs (3), (4), $exp\left(-\frac{J_w S}{D}\right)$ resolves ICP in association with structural parameter and $exp\left(\frac{J_w}{k}\right)$ resolves ECP in association with mass transfer coefficient.

S is the structural parameter of the support layer to diffusion within the porous support, determined by

$$\mathrm{S} = \frac{t_s \tau}{\varepsilon} \quad \text{(S5)}$$

where τ, t and ε are the tortuosity, thickness and porosity of the support layer.

mass transfer coefficient, k, is determined by eqs. (S6) and (S7). Eqs (S7) is valid only in laminar flow regime, which is applied for most membrane channel studies.

$$\mathrm{k} = \frac{ShD}{d_h} \quad \text{(S6)}$$

$$\mathrm{Sh} = 1.85(\mathrm{ReSc}\frac{d_h}{L})^{0.33} \quad \text{(S7)}$$

Where Sh, Re, Sc are sherwood number, reynolds number and schmidts number. d_h and L are hydraulic diameter and channel length. Eq. (7) is valid only in laminar flow regime, which is used in most membrane channel studies.

Irreversible thermodynamic model

Irreversible thermodynamic models [12,13] are rooted in four phenomenological coefficients and Onsager reciprocity relations[14]. General irreversible thermodynamic model can be expressed as below:

$$J_v = L_p \Delta p + L_{pD} \Delta \pi \quad \text{(S8)}$$

$$J_D = L_{Dp} \Delta p + L_D \Delta \pi \quad \text{(S9)}$$

$$L_{Dp} = L_{pD} \quad \text{(S10)}$$

where, J_v is the volumetric flux, J_D is the relative solute velocity to solvent, L_p is the volumetric transport coefficient, L_{Dp} and L_{pD} are the equivalent reciprocal coefficients from Onsager, and L_D is the diffusive solute transport coefficient.

When net flux through membrane is zero ($J_v = 0$) staverman reflection coefficient can be described by eq. (11). Using eq. (1) with null-flux condition eq. (S12) can be developed to obtain reciprocal coefficient.

$$\sigma = \left(\frac{\Delta P}{\Delta \pi}\right)_{J_v=0} (0 \leq \sigma \leq 1) \quad \text{(S11)}$$

$$\Delta \mathrm{P} = -\frac{L_{PD}}{L_P} \Delta \pi \quad \text{(S12)}$$

It should be noted that J_D is not solute flux ($\dot{n_s}$), which is more generally used for solute transport. Solute flux ($\dot{n_s}$) can be defined in terms of J_v, J_D and c_s in below eqs (S13)

$$\dot{n}_s = (J_v + J_D) c_s \quad (J_v = 0) \quad \text{(S13)}$$

Where c_s is concentration of solute in NaCl solution.

Under null-flux mode, $\mathrm{J_D}$ is naturally determined by normalizing solute flux with respective

316 NaCl concentration.

317

References

(1) Kim, B.; Gwak, G.; Hong, S. Review on Methodology for Determining Forward Osmosis (FO) Membrane Characteristics: Water Permeability (A), Solute Permeability (B), and Structural Parameter (S). Desalination 2017, 422 (February), 5–16. https://doi.org/10.1016/j.desal.2017.08.006.

(2) Zhang, H.; Cheng, S.; Yang, F. Use of a Spacer to Mitigate Concentration Polarization during Forward Osmosis Process. Desalination 2014, 347, 112–119. https://doi.org/10.1016/j.desal.2014.05.026.

(3) Wang, Y.; Zhang, M.; Liu, Y.; Xiao, Q.; Xu, S. Quantitative Evaluation of Concentration Polarization under Different Operating Conditions for Forward Osmosis Process. Desalination 2016, 398, 106–113. https://doi.org/10.1016/j.desal.2016.07.015.

(4) Suh, C.; Lee, S. Modeling Reverse Draw Solute Flux in Forward Osmosis with External Concentration Polarization in Both Sides of the Draw and Feed Solution. J. Memb. Sci. 2013, 427, 365–374. https://doi.org/10.1016/j.memsci.2012.08.033.

(5) Tan, C. H.; Ng, H. Y. Modified Models to Predict Flux Behavior in Forward Osmosis in Consideration of External and Internal Concentration Polarizations. J. Memb. Sci. 2008, 324 (1–2), 209–219. https://doi.org/10.1016/j.memsci.2008.07.020.

(6) Bui, N. N.; Arena, J. T.; McCutcheon, J. R. Proper Accounting of Mass Transfer Resistances in Forward Osmosis: Improving the Accuracy of Model Predictions of Structural Parameter. J. Memb. Sci. 2015, 492, 289–302. https://doi.org/10.1016/j.memsci.2015.02.001.

(7) Tiraferri, A.; Yip, N. Y.; Straub, A. P.; Romero-Vargas Castrillon, S.; Elimelech, M. A Method for the Simultaneous Determination of Transport and Structural Parameters of Forward Osmosis Membranes. J. Memb. Sci. 2013, 444, 523–538. https://doi.org/10.1016/j.memsci.2013.05.023.

(8) McCutcheon, J. R.; Elimelech, M. Influence of Concentrative and Dilutive Internal Concentration Polarization on Flux Behavior in Forward Osmosis. J. Memb. Sci. 2006, 284 (1–2), 237–247. https://doi.org/10.1016/j.memsci.2006.07.049.

(9) Kook, S.; Swetha, C. D.; Lee, J.; Lee, C.; Fane, T.; Kim, I. S. Forward Osmosis Membranes under Null-Pressure Condition: Do Hydraulic and Osmotic Pressures Have Identical Nature? Environ. Sci. Technol. 2018, 52 (6), 3556–3566. https://doi.org/10.1021/acs.est.7b05265.

(10) Lee, J.; Kook, S.; Lee, C.; Kim, I. S. Effect of Intermittent Pressure-Assisted Forward Osmosis (I-PAFO) on Organic Fouling. Desalination 2017, 419 (June), 60–69. https://doi.org/10.1016/j.desal.2017.06.003.

(11) Nguyen, T.-T.; Kook, S.; Lee, C.; Field, R. W.; Kim, I. S. Critical Flux-Based Membrane Fouling Control of Forward Osmosis: Behavior, Sustainability, and Reversibility. J. Memb. Sci. 2018, 570–571 (June 2018), 380–393. https://doi.org/10.1016/j.memsci.2018.10.062.

(12) Kedem, O.; Katchalsky, A. Thermodynamic Analysis of the Permeability of Biological Membranes to Non-Electrolytes. Biochim. Biophys. Acta 1958, 27, 229–246. https://doi.org/10.1016/0006-3002(58)90330-5.

(13) Spiegler, K. S.; Kedem, O. Thermodynamics of Hyperfiltration (Reverse Osmosis): Criteria for Efficient Membranes. Desalination 1966, 1 (4), 311–326. https://doi.org/10.1016/S0011-9164(00)80018-1.

(14) Onsager, L.; In, R. R.; Onsager, L.; In, R. R. RECIPROCAL RELATIONS IN IRREVERSIBLE PROCESSES. I. Phys. Rev. 1931, 37 (4), 405–426. https://doi.org/10.1103/PhysRev.37.405.